Journal of the Optical Society of America B
OPTICAL PHYSICS

Birefringence and piezo-Raman analysis of single crystal CVD diamond and effects on Raman laser performance

Hadiya Jasbeer,* Robert J. Williams, Ondrej Kitzler, Aaron McKay, Soumya Sarang, Jipeng Lin, and Richard P. Mildren

MQ Photonics Research Centre, Department of Physics and Astronomy, Macquarie University, Sydney, NSW 2109, Australia
**Corresponding author: hadiya.valiyaveettil-mohamm@students.mq.edu.au*

Received 1 October 2015; revised 21 December 2015; accepted 23 December 2015; posted 24 December 2015 (Doc. ID 251269); published 12 February 2016

Defect-induced stress has been mapped in optical-grade synthetic diamond (chemical vapor deposition grown, low nitrogen, low birefringence) using Metripol polarimetry, Mueller polarimetry, and Raman microscopy. Large circular retardance was observed in the 8 mm long ⟨110⟩ cut crystal with values up to 28° for some paths along the major axis. Metripol-determined values for linear birefringence magnitude and fast-axis direction in such regions have significant error. Stress-induced shifts in Raman frequency were observed up to 0.7 cm^{-1}, which we deduce result from uniaxial and biaxial stresses up to 0.86 GPa. We also elucidate the effect of stress on diamond Raman laser performance. For high cavity *Q* Raman lasers, the direction of the linear birefringence axis is found to be a primary factor determining the laser threshold and the input–output polarization characteristics.

OCIS codes: (140.4480) Optical amplifiers; (260.1440) Birefringence; (190.5650) Raman effect; (180.5655) Raman microscopy; (310.4925) Other properties (stress, chemical, etc.); (310.5448) Polarization, other optical properties.

http://dx.doi.org/10.1364/JOSAB.33.000B56

1. INTRODUCTION

Diamond is an extreme material that has a suite of properties of interest for applications in optics such as in nanophotonics and optomechanics, intracavity heat spreaders, high-power laser windows, synchrotron and x-ray optics, quantum information processing, and Raman lasers [1–9]. High thermal conductivity, a wide bandgap, high Raman gain, and a wide transmission window are a few of its outstanding properties pertinent to optical and photonic applications. In recent years, advances in synthesis by chemical vapor deposition (CVD) has enabled production of material with reduced impurity content and lower residual stress [10–12] and has been an important driving factor for a range of new optical applications. Nevertheless, stress in diamond, an isotropic crystal, plays an important role in influencing the behavior of polarization-sensitive devices [2,13,14]. To date, characterization of defect-induced stresses built in CVD diamonds have been reported using the Metripol method [12], a simple and widely used technique for characterizing the magnitude and direction of linear retardance [15,16]. However, Metripol is unable to detect other polarization properties, such as circular birefringence and dichroism, and its accuracy can be compromised if these other polarization characteristics are also present [16]. Stress also causes splitting and/or a shift in the spontaneous Raman line in crystals via the piezo-Raman effect [17–26]. A complete characterization of CVD diamond has not been reported in the literature to date, despite the fact that these are important for optimizing the performance of polarization-dependent diamond devices.

In this paper, we have characterized stress effects in optical-grade synthetic diamond using Mueller polarimetry, which provides a complete characterization of the polarization properties of the sample [27,28], and Raman microscopy. Significant circular retardance was observed in some locations within the diamond, causing significant inaccuracies in the Metripol-measured values for linear retardance. Raman microscopy was used to determine the magnitude of stress and its spatial distribution in the crystal. As an example of the effects of stress in an optical device, the diamond was investigated as the active medium in a continuous-wave (cw) Raman laser. The behavior was characterized for several locations in the diamond sample and correlated with the local birefringence characteristics.

2. CVD DIAMOND CHARACTERIZATION

A. Experimental Methods

1. Diamond Sample

The dimensions and crystallographic orientation of the diamond sample are illustrated in Fig. 1. The sample was an 8 × 4 × 1 mm CVD diamond (Raman-grade or "ultra-low birefringence," Element Six Ltd) with nitrogen impurity of approximately 20 ppb and birefringence $<10^{-5}$ perpendicular to the growth direction (indicated also in Fig. 1). This crystal was selected out of a batch of three as it contained the largest variation of birefringence features as viewed through the long direction of the sample. This direction is featured in our characterization as it is also the direction of beam propagation in the Raman laser experiments in Section 3.

2. Metripol and Mueller Polarimetry

The Metripol method was performed using an in-house system to determine both the magnitude and direction of linear retardance of the optical sample, the details of which are described in Ref. [16]. It consisted of a collimated, narrow-band, incoherent beam (in this case from an incandescent lamp, a 589 nm notch filter, and a collimating lens) passing through a rotatable polarizer, the optical sample, followed by a quarter-wave plate and an analyzing polarizer. The analyzing polarizer was set to 45° of the fast axis of the quarter-wave plate and a 10 cm focal length lens was used to image the end face of the diamond onto a CCD camera (Spiricon SP620U).

The normalized intensity of the transmitted light after passing through the diamond and the polarization elements is given by [16]

$$\frac{I}{I_0} = \frac{1}{2}[1 + \sin 2(\alpha - \Phi) \sin \delta], \quad (1)$$

where α is the polarizer rotation angle, Φ is defined as the angle between the linear retardance axis of the sample and the horizontal, and δ is the magnitude of linear retardance. The transmitted intensity as a function of rotatable polarizer angle is a sine curve whose amplitude is $\sin \delta$ and phase is Φ.

The polarizer was rotated in steps of 10°, and the transmitted light was captured by the CCD camera. The intensity recorded at each pixel, corresponding to a specific location in the diamond, was fitted to a sine curve as a function of α from which the amplitude and phase values were extracted to provide the magnitude and direction of linear retardance. We calculate the measurement uncertainty in linear retardance to be ±2.5° ($\Delta n = \pm 5 \times 10^{-7}$), due to imperfect polarizers and wave plates.

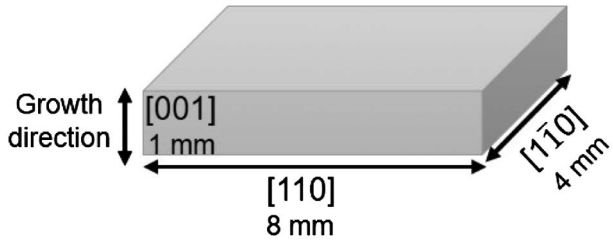

Fig. 1. Dimensions and crystallographic orientation of the diamond sample.

Mueller polarimetry, the principles of which are described in Ref. [27], was performed using a commercially available Mueller polarimeter (Exicor 150 XT from Hinds Instruments). The instrument launches a variety of known polarization states from a He–Ne laser (operating at 632.8 nm), polarizer, and computer-controlled polarization modulating photoelastic elements. The modulated light passes through the length of the sample whose polarization is further modulated by the birefringence in the sample. The instrument uses another pair of photoelastic modulators along with a polarizer, and photodetector to analyze the transmitted state of polarization from the sample under test corresponding to each launched state of polarization. Through the Mueller analysis of the recorded data (Ref. [27]), the system calculates all sixteen Mueller matrix elements of the sample under test. Metripol and Mueller polarimetry are based on intensity variations as a function of polarization and are therefore unaffected by scatter and absorption in diamond. Dichroism is found to be negligible in all cases.

3. Raman Microscopy

Raman spectra were recorded as a function of position in the sample using a confocal microscope equipped with a Raman spectrometer (Renishaw RM1000 Micro-Raman spectrometer). A 2400 lines/mm grating and 50 μm slit provided 5 cm^{-1} spectral resolution. The excitation source was a frequency-doubled Nd:YAG laser with 532 nm output. A 50 × objective lens with N.A. 0.75 provided a 1 μm probe beam spot size. A motorized stage was used to raster the sample in the X–Y plane in 25 μm step. To accurately determine the Raman shifts at each point in the crystal, each spectrum was fitted using a Gaussian function, thus enabling greatly enhanced resolution of the peak shift measurement to 0.17 cm^{-1}. Furthermore, averaging over many pixels in a particular region of interest increased the effective resolution of the peak position measurement to approximately 50–100 times greater than the Raman linewidth (depending on the chosen sample area for averaging), thus enabling very small shifts to be resolved.

B. Results and Discussion

1. Linear and Circular Birefringence

Figures 2(a) and 2(b) show maps of the magnitude and direction of linear retardance through the 1 × 4 mm end face obtained using Metripol and Mueller polarimetry. The qualitative features from the two methods are similar, showing a complex birefringence pattern across the sample. Both measurements reveal extended features in the growth direction in the central region of the crystal, and to the right of center, with linear retardance up to 55° (Δn up to 1.2×10^{-5}) as measured using Mueller polarimetry and up to 50° using Metripol. The values obtained using Mueller are systematically higher or lower than for Metripol, due to the contribution of circular retardance as discussed below. The direction of linear retardance likewise varies markedly across the sample from −90° to +90° showing some correlation with the linear retardance maps. Also, as with the magnitude of linear retardance, the orientations obtained using Mueller depart significantly from those obtained with Metripol in the central region of the crystal. Figure 2(c) shows the circular retardance map measured

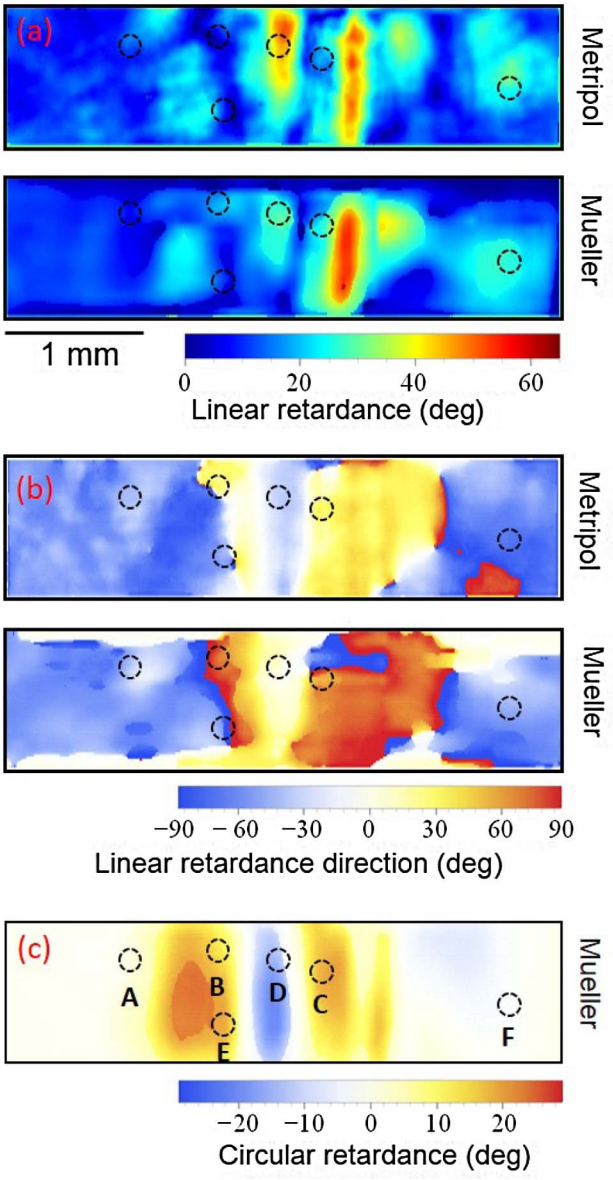

Fig. 2. Metripol and Mueller polarimetry-obtained values of (a) linear retardance magnitude and (b) direction. (c) Circular retardance obtained from Mueller polarimetry. Positive and negative values correspond to dextro and levo rotation, respectively. 0° represents the [1$\bar{1}$0] (horizontal in figure) direction. The black circles A, B, C, D, E, and F mark the six regions that were characterized under Raman laser operation. The circle (0.3 mm diameter) indicates the uncertainty in location of the laser spot.

using Mueller polarimetry. Significant circular retardance of up to 28° was measured at different locations in the sample. Some circular retardance is expected as the equivalent optical element for the path through a medium with varying magnitude and direction of linear retardance can be reduced to a single waveplate and rotator [29,30]. It is interesting, however, that the magnitude of circular retardance is up to approximately half of the maximum linear retardance observed in the crystal. Of the other polarization characteristics measured using Mueller polarimetry (e.g., linear and circular dichroism), none were detected in significant quantities in this sample.

2. Effect of Circular Retardance on Metripol Measurements

In order to quantify the effect of circular retardance on the accuracy of the Metripol-determined linear retardance, we introduce circular retardance χ into the Jones matrix of the sample under test, which for $\chi < \delta/2$ can be expressed as [16]

$$M = \begin{bmatrix} e^{\frac{i\delta}{2}} & -2\chi\frac{\sin\frac{\delta}{2}}{\delta} \\ 2\chi\frac{\sin\frac{\delta}{2}}{\delta} & e^{\frac{-i\delta}{2}} \end{bmatrix}. \tag{2}$$

Thus, the Jones matrix that describes the transmitted intensity through the entire Metripol setup becomes

$$A'' = \frac{1}{2}\begin{bmatrix} 1 & 1 \\ 1 & 1 \end{bmatrix}\begin{bmatrix} e^{\frac{i\pi}{4}} & 0 \\ 0 & e^{\frac{-i\pi}{4}} \end{bmatrix}\begin{bmatrix} e^{\frac{i\delta}{2}} & -2\chi\frac{\sin\frac{\delta}{2}}{\delta} \\ 2\chi\frac{\sin\frac{\delta}{2}}{\delta} & e^{\frac{-i\delta}{2}} \end{bmatrix} \times \begin{bmatrix} \cos\theta & \sin\theta \\ -\sin\theta & \cos\theta \end{bmatrix}\begin{bmatrix} 1 \\ 0 \end{bmatrix}, \tag{3}$$

where

$$\theta = \alpha - \Phi. \tag{4}$$

In this case, when the normalized intensity of the exiting beam is plotted against the rotation angle of the polarizer, there is a change in amplitude and phase of the sine curve which in turn affects the Metripol-measured magnitude and direction of linear retardance. Figure 3 shows the shift in magnitude and direction of linear retardance with circular retardance. The magnitude and direction of linear retardance increases with positive circular retardance and decreases with negative circular retardance. For example, for a region in the diamond having maximum linear retardance magnitude of 55° oriented at 75° and circular retardance of 25°, the Metripol-determined values for the magnitude and orientation of the linear retardance are 53° and 60°, respectively. Accordingly, in the Metripol birefringence map of Fig. 2(a), areas that have significant circular birefringence have errors attributable to circular birefringence of up to 5° in magnitude and 27° in orientation. In the central region of the crystal (the region of the crystal marked as D), the Metripol-determined values of magnitude and direction of linear retardance is found to be higher than Mueller-determined values because of negative circular retardance in this area as is evident from Fig. 3.

3. Birefringence and Piezo-Raman Effects for the (001) Face

In order to elucidate the cause of birefringence observed through the [110] face, the stress pattern for the major face of the crystal was revealed using Metripol polarimetry and Raman microscopy, as shown in Fig. 4. The Metripol polarimetry technique was used here as we were primarily interested in the stress distribution through the [110] face rather than the details of each Mueller matrix component. The linear and circular birefringence of Fig. 2 is the result of the integrated effect of stressed regions distributed along the 8 mm length. The magnitude of linear retardance [Fig. 4(a)] shows a complex pattern with values up to 60°. This corresponds to Δn values up to 1.1×10^{-4} which, as expected for the line-of-sight along the growth direction, is an order of magnitude higher than in the perpendicular direction [10,12]. Again, the magnitude

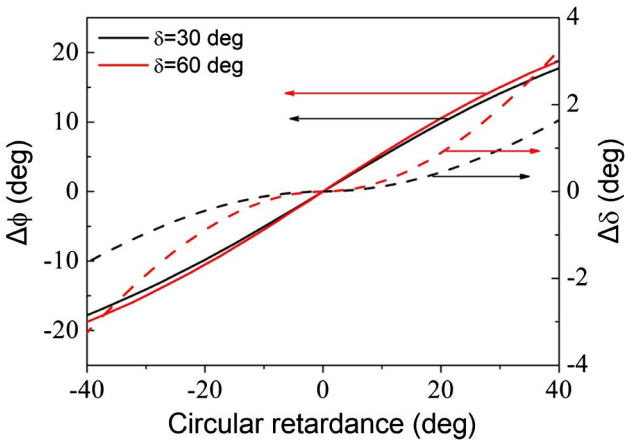

Fig. 3. Shift in Metripol-measured magnitude and direction of linear retardance as a function of circular retardance. Black and red solid lines indicate the shift in linear retardance direction with circular retardance for $\delta = 30°$ and $\delta = 60°$, respectively. Black and red dashed lines indicate the shift in linear retardance magnitude with circular retardance for $\delta = 30°$ and $\delta = 60°$, respectively.

and direction maps show some correlation. Stress features aligned along the [010] direction are observed on the left-hand side of the image. A notable feature with twofold symmetry is observed on the right-hand side slightly above center.

Stress may also cause splitting and/or a shift in the Raman line in crystals [17–26] depending upon the magnitude of the stress tensor components. Figure 4(c) shows the Raman frequency shift for backscattering along the [001] direction. No broadening of the peak is observed within the measurement uncertainty, indicating that the sampling volume is smaller than the granularity of the stress pattern. The shift in Raman peak is calculated with respect to the minimum stress value obtained at the bottom left-hand side of the birefringence map. A similar map is obtained for the laser focused 0.5 mm below the sample surface, indicating that the map is representative of the stress field throughout the 1 mm thick sample. Positive and negative shifts in frequency were observed, but the individual spectra showed no splitting of the Raman line. This is consistent with the polarization selection rules for Raman scattering, where only a singlet peak is observed for backscattering from a (001) surface in the cases of uniaxial or biaxial stresses acting in the (001) plane [19]. In diamond, positive and negative shifts correspond to compressive stress and tensile stress, respectively [23,26,31]. The Raman frequency map contains features that correspond to the two main features in the Metripol images; stress features that are elongated in the [010] and [100], and a region of large frequency shift that coincides with the twofold symmetric pattern (in the right-hand side above center). It is interesting to note that this latter region has the largest frequency shift while having relatively low birefringence. The peak shift is $+0.7\ \mathrm{cm}^{-1}$, which is approximately half the Raman linewidth in diamond, $1.5\ \mathrm{cm}^{-1}$ [32–34]. On average along the length of the crystal, the magnitude of the shift is less than $0.13\ \mathrm{cm}^{-1}$. Since this is a small fraction of the Raman linewidth of diamond and the region only occupies a minor portion of the total length, we do not expect a

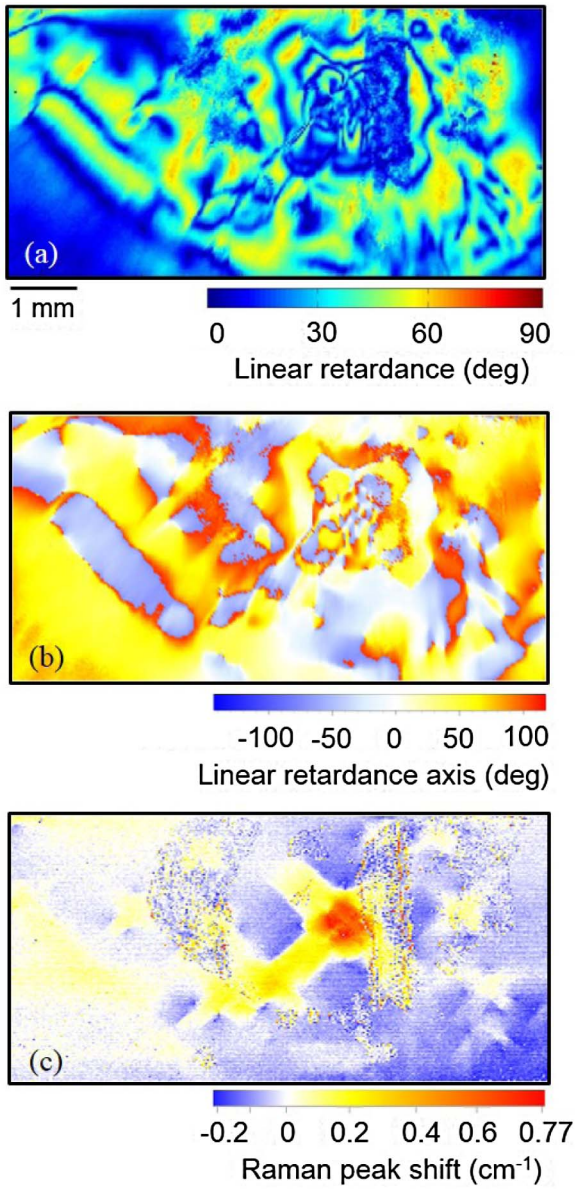

Fig. 4. (a),(b) Magnitude and direction of linear retardance across (001) plane obtained from Metripol (0° represents [110] direction), and (c) Raman peak shift map measured by backscattering from the (001) plane.

significant stress-induced decrease in the Raman gain of this crystal for beams propagating along [110].

The correspondence between birefringence and Raman frequency shift can be understood by considering the piezo-Raman and piezo-optic tensor in diamond. The change in dielectric impermittivity due to an applied stress σ_{ij} is given by [35]

$$\zeta_{ij} = \pi_{ijkl}\sigma_{kl} \qquad i,j,k,l = 1,2,3, \tag{5}$$

where π_{ijkl} is the fourth-rank piezo-optic tensor. For a biaxial stress, Eq. (5) (in the abbreviated notation) becomes

$$\zeta_\lambda = \begin{bmatrix} \pi_{11} & \pi_{12} & \pi_{12} & 0 & 0 & 0 \\ \pi_{12} & \pi_{11} & \pi_{12} & 0 & 0 & 0 \\ \pi_{12} & \pi_{12} & \pi_{11} & 0 & 0 & 0 \\ 0 & 0 & 0 & \pi_{44} & 0 & 0 \\ 0 & 0 & 0 & 0 & \pi_{44} & 0 \\ 0 & 0 & 0 & 0 & 0 & \pi_{44} \end{bmatrix} \begin{bmatrix} \sigma_{11} \\ \sigma_{22} \\ 0 \\ 0 \\ 0 \\ 0 \end{bmatrix} \tag{6}$$

$$= \begin{bmatrix} \sigma_{11}\pi_{11} + \sigma_{22}\pi_{12} \\ \sigma_{11}\pi_{12} + \sigma_{22}\pi_{11} \\ \sigma_{11}\pi_{12} + \sigma_{22}\pi_{12} \\ 0 \\ 0 \\ 0 \end{bmatrix}, \tag{7}$$

where the birefringence Δn is given in terms of ζ_λ as

$$\Delta n = \left(n_0 - \frac{n_0^3}{2}\zeta_1\right) - \left(n_0 - \frac{n_0^3}{2}\zeta_2\right), \tag{8}$$

which when viewing along [001] becomes

$$\Delta n = \frac{n_0^3}{2}(\sigma_{22} - \sigma_{11})(\pi_{11} - \pi_{12}). \tag{9}$$

Thus, the birefringence due to biaxial stress is proportional to the difference between the stress components σ_{11} and σ_{22}.

In contrast, the shift in Raman frequency $\Delta\omega_R$ due to biaxial stress is proportional to the sum of the stress components [20]:

$$\Delta\omega_R = \frac{1}{2\omega_0}[(\sigma_{11} + \sigma_{22})(pS_{12} + q(S_{11} + S_{12}))] \tag{10}$$

$$= -8.1576 \times 10^{-10}(\sigma_{11} + \sigma_{22}), \tag{11}$$

where p and q are the phonon deformation potentials, and S_{11} and S_{12} are the elastic compliance tensor components. Evaluation of Eq. (11) enables the stress values to be determined. The values of p and q were calculated from the mode Gruneisen parameter γ_G and the factor $(p - q)/2\omega_0^2$ given in Ref. [36]. The values of S_{11} and S_{12} were calculated from the elastic stiffness constants C_{11} and C_{12} given in Ref. [37]. The maximum frequency shift of $+0.7$ cm^{-1} corresponds to biaxial stress $(\sigma_{11} + \sigma_{22})$ of 0.86 GPa. Regions of the crystal with negative frequency shift indicate the action of tensile biaxial stress.

Hence, the region of low Δn and high $\Delta\omega_R$ of the twofold symmetric pattern is consistent with a transversely isotropic stress field (σ_{11} approximately equal to σ_{22}) in the (100) plane. For uniaxially stressed regions (σ_{11} or σ_{22} approximately equal to 0), $\Delta\omega_R$ increases with Δn which is consistent with scenarios on the left-hand side of the crystal.

3. EFFECTS ON RAMAN LASER BEHAVIOR

The combination of diamond's high Raman gain coefficient, damage threshold, and thermal conductivity, along with its low thermal expansion coefficient and wide transmission band, has led to the development of Raman lasers featuring outstanding output power capability approaching kW [13], high efficiency [38–43], and wide wavelength operating range [7,42,44–46]. However, understanding absorption losses and impurities, especially those of nitrogen, is important to laser design and optimization [7]. In cw Raman lasers in particular, minimization of intracavity losses is crucial to attaining high efficiency [7,10] due to their typically lower gain compared to pulsed devices. Recently, the presence of small amounts of birefringence has also been found to perturb performance. Furthermore, the polarization behavior of cw Raman lasers has been found to substantially deviate from that predicted from the Raman tensors, an effect that has been proposed to be due to stress-induced birefringence in the diamond [13,14]. In order to gain a more complete picture of Raman laser optimization, the effect of birefringence on laser performance is investigated here in detail.

The Raman gain coefficient is dependent on pump and Stokes polarizations according to [47]

$$g_s = k\sum_{i=1}^{3}(e_p R_i e_s)^2, \tag{12}$$

where the Raman tensor components R_1, R_2, and R_3 correspond to triply degenerate F_{2g} vibrational modes of diamond [48], and e_p and e_s are the pump and Stokes polarization unit vectors, respectively. The proportionality constant k is given by $k = 4\pi^2 N\omega_s/n_s n_p c_0^2 m\omega_R\Gamma$, where N is the number density of molecules, ω_s is the angular frequency of the Stokes photons, n_s and n_p are the refractive indices of diamond at the Stokes and pump frequencies, respectively, c_0 is the speed of light in vacuum, m is the reduced mass, and Γ is the Raman linewidth.

The Raman gain as a function of pump and Stokes polarizations for beam propagation along the [110] direction is shown in Fig. 5. The following behavior is shown: for a ⟨110⟩-polarized pump (labeled X in Fig. 5), the gain is uniform for all Stokes polarizations. For small angles of pump polarization, the gain has a maximum for a Stokes polarization near 45°. This angle counter-rotates as the pump polarization angle is increased. For a pump polarization of ⟨111⟩, the Stokes polarization is collinear and the Raman gain attains its maximum value. Upon further rotation of the pump polarization, the Stokes polarization continues to rotate until at X there is a flip in the Stokes polarization of 90°. Such polarization dynamics have been observed previously in a low-Q diamond Raman laser pumped with nanosecond pulses [41] and in similar lasers [40] investigated by some of the present authors when using diamond samples from the same batch and possessing similar birefringence characteristics to the sample used in this report. In these lasers, birefringence is not observed to influence the output Stokes polarization. However, for cw diamond Raman lasers in which the cavity Q is typically much higher, the circulating Stokes field experiences a large number of round trips before coupling out of the resonator. As a result, the influence of diamond birefringence on the polarization of the Stokes beam is increased leading to a substantial perturbation of the output polarization from that predicted by the Raman tensors [13,14].

A. Experiment

The Raman laser threshold, Stokes output polarization, and pump depolarization were studied as a function of pump polarization for areas of the diamond sample that provide a range of birefringence properties. Note that our current sample

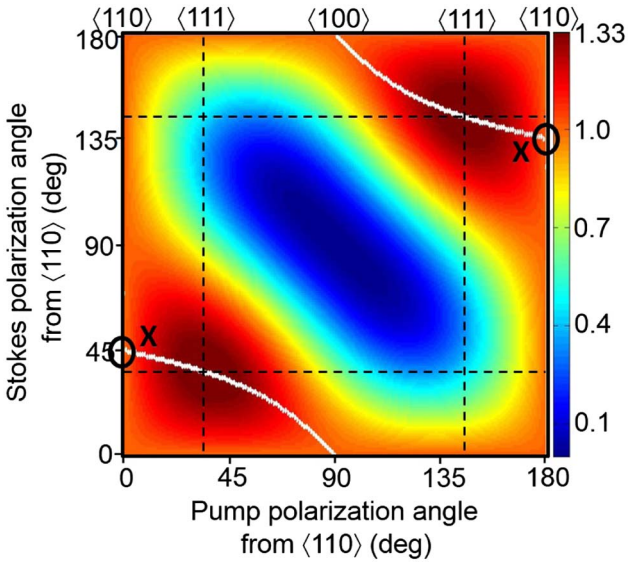

Fig. 5. Normalized Raman gain coefficient for propagation along the ⟨110⟩ direction as a function of pump and Stokes polarizations. Notable directions in diamond are represented by black dashed lines, and the maximum scattering efficiency amplitude is shown by the white loci.

under test is of the same type as that typically used in previous reports of cw diamond Raman lasers [13,14,38,39]

The diamond was placed on an X–Y–Z translation stage, allowing different regions in the crystal to be investigated. An IR camera was used to monitor the pump spot in the diamond in order to correlate the position in the diamond with the birefringence map, with an accuracy of 0.3 mm. The six regions marked A, B, C, D, E, and F in Fig. 2 were selected as these provided a range of δ, Φ, and χ values and was a sufficiently large set to characterize the observed features in polarization behavior. Regions A and F have the least amount of circular retardance (2°); B, C, D, and E have circular retardance of 12°, 19°, −13°, and 17°, respectively, as shown in Fig. 2. The magnitudes and directions of linear and circular retardance are summarized in Table 1.

Figure 6 shows the experimental setup providing simultaneous characterization of the Stokes polarization, lasing threshold, and pump depolarization. The pump source was a quasi-cw-pumped Nd:YAG laser with horizontally polarized output at 1064 nm, operating at 40 Hz repetition rate and 1% duty cycle (pulse duration approximately 250 μs). Variable attenuation of the pump beam was achieved with a rotatable half-wave plate and a polarizing cube. The diamond laser cavity was a 104 mm long near-concentric resonator consisting of concave mirrors with 50 mm radii of curvature. The input coupler was highly transmitting (>97%) at the pump and highly reflecting (99.98%) at the 1240 nm first Stokes. The output coupler was highly reflecting at the pump and provided 0.4% transmission at the first Stokes output wavelength. The antireflection-coated diamond was placed in the center of the cavity. A 50 mm focusing lens was used to focus the pump beam into the middle of the diamond. A half-wave plate (HWP 1 in Fig. 6) was used to rotate the injected pump polarization. In the following sections, the polarization angles are quoted with respect to the ⟨110⟩ direction. The total output Stokes power was monitored using an InGaAs photodiode (PD 1 in Fig. 6), while the degree and orientation of the Stokes polarization were determined using a half-wave plate and cube polarizer (rotating the half-wave plate and measuring the extinction). The depolarized pump power was monitored as a function of injected pump polarization as a check of the linear retardance axis measured using the Metripol technique and verifying the region in the diamond with respect to the birefringence map. This was achieved by removing the input coupler and measuring the backreflected, depolarized pump power on a photodetector.

B. Results

Figure 7 shows the output Stokes polarization (top row), measured and calculated threshold (middle row), and pump depolarization (bottom row) as a function of pump polarization for the four out of six regions shown in Fig. 2. The four regions A–D were selected as they were representative of the polarization behavior seen in all regions. The Stokes polarization, threshold, and pump depolarization for all the six regions investigated are given in Table 1. In each case, the Stokes polarization remains fixed to either of two orthogonal linear polarizations depending on the pump polarization. For all regions except D, the Stokes polarization is observed to switch between the orthogonal polarizations at a point in the cycle. The switching points, and the polarization directions, vary substantially for each region. The threshold for the different regions ranges from 18 to 55 W.

Table 1. Summary of the Magnitude and Direction of Linear and Circular Retardance (Measured Using Metripol and Mueller Polarimetry), Pump Depolarization, Stokes Polarization, and Minimum Threshold for the Crystal Locations A, B, C, D, E, and F Indicated in Fig. 2

	Region A	Region B	Region C	Region D	Region E	Region F
Δn (Metripol)	1.4×10^{-6}	2.5×10^{-6}	4.5×10^{-6}	7.2×10^{-6}	2.2×10^{-6}	4.8×10^{-6}
Δn (Mueller)	1.6×10^{-6}	3.9×10^{-6}	5.3×10^{-6}	6.7×10^{-6}	3.1×10^{-6}	5.2×10^{-6}
Principle axis (Metripol)	40°	40°	46°	26°	43°	41°
Principle axis (Mueller)	45°	59°	71°	1.7°	59°	37°
Circular retardance (Mueller)	2.5°	12°	18.3°	−13.2°	17°	2°
Depolarization axes	—	40°	50°	30°	40°	40°
Stokes polarization	45° and 135°	50° and 140°	62° and 152°	178°-no flip	52° and 142°	34° and 124°
Minimum threshold	18 W	24 W	25 W	53.5 W	27 W	28 W

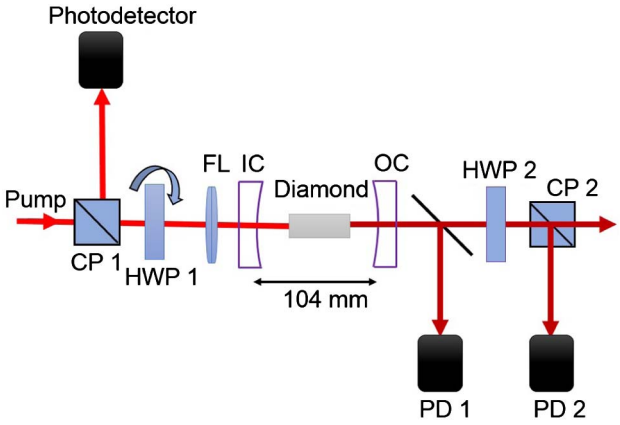

Fig. 6. Experimental arrangement for measuring laser threshold and polarization characteristics: CP, cube polarizer; HWP, half-wave plate; FL, focusing lens; IC, input coupler; OC, output coupler; PD, photodiode.

For region A, which has low circular retardance (2.5°), the linear birefringence axes obtained from Metripol (40°) and Mueller (46°) are in fair agreement. The two Mueller-obtained axes values closely match the two orthogonal Stokes polarizations (45° and 135°). A similar behavior is also observed for region F (Table 1). No significant pump depolarization was observed for region A as expected because of the low linear birefringence value ($\Delta n = 1.6 \times 10^{-6}$).

Regions B and C have significant circular retardance which substantially perturbs the Metripol-determined linear retardance direction. The direction obtained using the pump depolarization measurement matches the Metripol measurement as expected, since both measurements are unable to deconvolve the contributions of circular and linear retardance. For both the regions, the Stokes polarizations have directions closer to the Mueller-determined linear retardance axis. From Table 1, it can be seen that region E shows a similar behavior.

As for B and C, region D has large circular retardance and thus also a large difference between the linear retardance directions obtained using Metripol (24°) and Mueller (2°) polarimetry. However, as the circular retardance is negative, the Metripol-determined axis direction is overvalued in this case. Region D is also unique in that the output Stokes polarization state is constant at 178° for all pump polarizations. The reason for this is explained in the following section.

C. Analysis and Discussion

The above results reveal that the Stokes polarization is fixed to either of the axes of linear retardance. This is in stark contrast to the case of low-Q (nanosecond-pulsed) diamond Raman lasers whose polarization dynamics are dictated purely by the Raman tensors. In regions of large circular retardance, it is found that Mueller polarimetry is more suitable for predicting the output Stokes polarization.

Using the measured directions of the lasing Stokes polarizations, we have calculated the Raman laser threshold as a function of pump polarization according to the scattering efficiency [Eq. (12)]. The middle row of Fig. 7 shows the measured threshold (red and black rectangular markers) and calculated threshold using the observed Stokes polarizations. The calculated threshold has been scaled to the measured threshold to account for variations in diamond coating losses, surface quality, and cavity alignment.

It is seen that the Stokes polarization is fixed to the retardance axis that provides the highest gain according to the injected pump polarization. For example, for A, the threshold

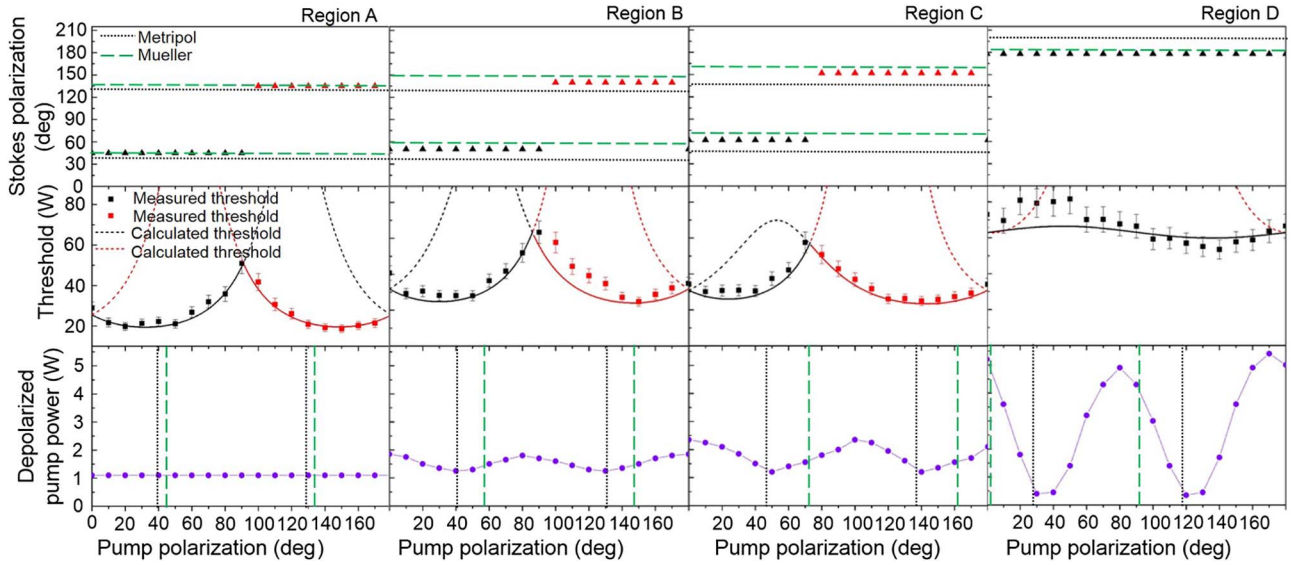

Fig. 7. Laser properties as a function of pump polarization for regions A, B, C and D. Top row: Stokes polarization (black and red triangular marker) along with the linear retardance axis direction obtained by Metripol (black dotted line) and Mueller (green dashed line). Middle row: threshold for the two orthogonal Stokes polarizations measured (black and red rectangular markers) and calculated (black and red dashed and solid lines). The solid lines indicate the calculated threshold corresponding to the polarization state with the highest Raman gain. Bottom row: pump depolarization (violet circular markers). As for the top row, the Metripol- and Mueller-measured linear retardance axis directions are shown.

for 45° Stokes polarization is less than the threshold for 135° for pump polarizations in the range 0° to 91°, whereas the threshold for 135° Stokes polarization is less than for 45° for pump polarizations in the range 92° to 180°. Hence, we observe that the output polarization switches between birefringence axis directions according to which has the highest gain. The same behavior is observed for B and C (also for E and F). For D, the threshold for 178° Stokes polarization is less than its orthogonal Stokes polarization over the entire range of pump polarization angles consistent with the absence of a transition in the measured Stokes polarization.

The maximum scattering efficiencies for A, B, C, E, and F are of a similar magnitude as their birefringence axes are closely oriented to a ⟨111⟩ crystal direction. This is consistent with the similar minimum threshold for these five regions (18–28 W). The minimum threshold for D (50 W) is notably higher, partially due to the Stokes polarization being well away from the direction of maximum scattering efficiency. Note that slight variations in the coating and surface quality at each location, as well as precise alignment (which affects the pump/Stokes mode overlap), also contribute to the spread of observed thresholds.

These results show that weak stress-induced birefringence in the diamond crystal ($\Delta n \sim 10^{-6}$) affects the performance of cw diamond Raman lasers (DRLs), fixing the Stokes output polarizations to the local birefringence axes and thereby determining the maximum Raman gain coefficient achievable as a function of pump polarization. As the Stokes polarization is fixed to the local linear birefringence axis, pumping along ⟨111⟩ no longer provides maximum gain in all cases but only when Stokes polarization is aligned to ⟨111⟩. Hence, if the birefringence axis is not parallel to ⟨111⟩, the gain coefficient is less than the maximum achievable. Our results, for regions A–F and all other regions investigated, show no clear correlation between the magnitude of linear or circular retardance and DRL performance.

4. CONCLUSIONS

Here we have characterized the birefringence properties of single-crystal, CVD diamond and elucidated the effects of birefringence on cw Raman lasers. The sample showed significant circular birefringence in addition to linear birefringence, and thus the Mueller technique is a more appropriate tool for characterizing the birefringence magnitude and direction of CVD diamonds. We observed uniaxial and biaxial stresses in the (001) plane leading to shifts in the Raman line up to 0.7 cm^{-1} and corresponding to stress values up to 0.86 GPa.

We have shown that the Stokes polarization in cw Raman lasers is fixed to the local birefringence axes, in contrast to nanosecond-pulsed diamond Raman lasers for which the Stokes polarization follows the maximum Raman scattering efficiency predicted by Raman tensors. The greater susceptibility of cw devices to birefringence is attributed to the much greater number of round trips for the Stokes beam through the diamond medium. Since the Raman gain is dependent on both pump and Stokes polarizations, the Raman gain is maximized for locations in diamond where the retardance axis and pump polarization is aligned close to the ⟨111⟩ direction. These results have implications for optimizing high-Q cavity diamond Raman lasers and are expected to provide insights into the performance and optimization of other diamond-based optical devices.

Funding. ARC Discovery Grants (DP130103799, DP150102054); Air Force Research Laboratory (AFRL) (FA2386-15-1-4075); Macquarie University Research Excellence Scholarship; Macquarie University Research Fellowship.

Acknowledgment. The authors thank Hinds Instruments for the Mueller polarimetry measurements and Krystyna Drozdowicz-Tomsia for her assistance with the Raman microscope. H. Jasbeer received a Macquarie University Research Excellence Scholarship (2013). R. J. Williams received a Macquarie University Research Fellowship (2015).

REFERENCES

1. R. S. Balmer, J. R. Brandon, S. L. Clewes, H. K. Dhillon, J. M. Dodson, I. Friel, P. N. Inglis, T. D. Madgwick, M. L. Markham, T. P. Mollart, N. Perkins, G. A. Scarsbrook, D. J. Twitchen, A. J. Whitehead, J. J. Wilman, and S. M. Woollard, "Chemical vapour deposition synthetic diamond: materials, technology and applications," J. Phys. **21**, 364221 (2009).
2. F. van Loon, A. J. Kemp, A. J. Maclean, S. Calvez, J.-M. Hopkins, J. E. Hastie, M. D. Dawson, and D. Burns, "Intracavity diamond heat-spreaders in lasers: the effects of birefringence," Opt. Express **14**, 9250–9260 (2006).
3. D. H. Douglas-Hamilton, E. D. Hoag, and J. R. M. Seitz, "Diamond as a high-power-laser window," J. Opt. Soc. Am. **64**, 36–38 (1974).
4. B. J. M. Hausmann, I. B. Bulu, P. B. Deotare, M. McCutcheon, V. Venkataraman, M. L. Markham, D. J. Twitchen, and M. Lončar, "Integrated high-quality factor optical resonators in diamond," Nano Lett. **13**, 1898–1902 (2013).
5. B. J. M. Hausmann, T. M. Babinec, J. T. Choy, J. S. Hodges, S. Hong, I. Bulu, A. Yacoby, M. D. Lukin, and M. Lončar, "Single-color centers implanted in diamond nanostructures," New J. Phys. **13**, 045004 (2011).
6. B. J. M. Hausmann, M. Khan, Y. Zhang, T. M. Babinec, K. Martinick, M. McCutcheon, P. R. Hemmer, and M. Lončar, "Fabrication of diamond nanowires for quantum information processing applications," Diam. Relat. Mater. **19**, 621–629 (2010).
7. R. P. Mildren, A. Sabella, O. Kitzler, D. J. Spence, and A. M. McKay, "Diamond Raman laser design and performance," in *Optical Engineering of Diamond*, R. P. Mildren and J. R. Rabeau, eds. (Wiley-VCH Verlag GmbH, 2013), pp. 239–276.
8. A. K. Freund, J. Friedel Sellschop, K. Lieb, S. Rony, S.-B. Clemens, L. Schroeder, and J. Teyssier, "Recent diamond single crystal x-ray optics developments at the European synchrotron radiation facility," Proc. SPIE **3448**, 53–63 (1998).
9. O. J. L. Fox, L. Alianelli, A. M. Malik, I. Pape, P. W. May, and K. J. S. Sawhney, "Nanofocusing optics for synchrotron radiation made from polycrystalline diamond," Opt. Express **22**, 7657–7668 (2014).
10. I. Friel, S. L. Geoghegan, D. J. Twitchen, and G. A. Scarsbrook, "Development of high quality single crystal diamond for novel laser applications," Proc. SPIE **7838**, 783819 (2010).
11. I. Friel, "Optical quality diamond grown by chemical vapor deposition," in *Optical Engineering of Diamond*, R. P. Mildren and J. R. Rabeau, eds. (Wiley-VCH Verlag GmbH, 2013), pp. 35–69.
12. I. Friel, S. Clewes, H. Dhillon, N. Perkins, D. Twitchen, and G. Scarsbrook, "Control of surface and bulk crystalline quality in single crystal diamond grown by chemical vapour deposition," Diam. Relat. Mater. **18**, 808–815 (2009).
13. R. J. Williams, O. Kitzler, A. McKay, and R. P. Mildren, "Investigating diamond Raman lasers at the 100 W level using quasi-continuous-wave pumping," Opt. Lett. **39**, 4152–4155 (2014).

14. O. Kitzler, "External cavity diamond Raman lasers for high-power continuous-wave beam conversion," Ph.D. thesis (Macquarie University, 2014).
15. A. M. Glazer, J. G. Lewis, and W. Kaminsky, "An automatic optical imaging system for birefringent media," Philos. Trans. R. Soc. London Ser. A **452**, 2751–2765 (1996).
16. W. Kaminsky, K. Claborn, and B. Kahr, "Polarimetric imaging of crystals," Chem. Soc. Rev. **33**, 514–525 (2004).
17. F. Cerdeira, C. J. Buchenauer, F. H. Pollak, and M. Cardona, "Stress-induced shifts of first-order Raman frequencies of diamond-and zinc-blende-type semiconductors," Phys. Rev. B **5**, 580–593 (1972).
18. E. Anastassakis, A. Cantarero, and M. Cardona, "Piezo-Raman measurements and anharmonic parameters in silicon and diamond," Phys. Rev. B **41**, 7529–7535 (1990).
19. Y. von Kaenel, J. Stiegler, J. Michler, and E. Blank, "Stress distribution in heteroepitaxial chemical vapor deposited diamond films," J. Appl. Phys. **81**, 1726–1736 (1997).
20. I. De Wolf, "Relation between Raman frequency and triaxial stress in Si for surface and cross-sectional experiments in microelectronics components," J. Appl. Phys. **118**, 053101 (2015).
21. M. H. Grimsditch, E. Anastassakis, and M. Cardona, "Effect of uniaxial stress on the zone-center optical phonon of diamond," Phys. Rev. B **18**, 901–904 (1978).
22. J. W. Ager and M. D. Drory, "Quantitative measurement of residual biaxial stress by Raman spectroscopy in diamond grown on a Ti alloy by chemical vapor deposition," Phys. Rev. B **48**, 2601–2607 (1993).
23. A. Crisci, F. Baillet, M. Mermoux, G. Bogdan, M. Nesládek, and K. Haenen, "Residual strain around grown-in defects in CVD diamond single crystals: a 2D and 3D Raman imaging study," Phys. Status Solidi A **208**, 2038–2044 (2011).
24. K. E. Bennet, K. H. Lee, J. R. Tomshine, E. M. Sundin, J. N. Kruchowski, W. G. Durrer, B. M. Manciu, A. Kouzani, and F. S. Manciu, "Raman microscopic analysis of internal stress in boron-doped diamond," Materials **8**, 2782–2793 (2015).
25. H. Boppart, J. Van Straaten, and I. F. Silvera, "Raman spectra of diamond at high pressures," Phys. Rev. B **32**, 1423–1425 (1985).
26. E. J. D. Liscia, F. Alvarez, E. Burgo, E. Halac, H. Huck, and M. Reinoso, "Stress analysis on single-crystal diamonds by Raman spectroscopy 3D mapping," Mater. Sci. Appl. **4**, 191–197 (2013).
27. O. Arteaga, J. Freudenthal, B. Wang, and B. Kahr, "Mueller matrix polarimetry with four photoelastic modulators: theory and calibration," Appl. Opt. **51**, 6805–6817 (2012).
28. J. L. Pezzaniti, "Mueller matrix imaging polarimetry," Opt. Eng. **34**, 1558–1568 (1995).
29. L. S. Srinath and A. V. S. S. S. R. Sarma, "Effects of stress-induced optical activity in photoelasticity," J. Phys. D **5**, 883–895 (1972).
30. V. Yu, "Symmetry conditions for studying torsion stress-induced gradient piezogyration," Ukr. J. Phys. Opt. **14**, 91–95 (2013).
31. H. Kagi, S. Odake, S. Fukura, and D. A. Zedgenizov, "Raman spectroscopic estimation of depth of diamond origin: technical developments and the application," Russ. Geol. Geophys. **50**, 1183–1187 (2009).
32. R. P. Mildren, "Intrinsic optical properties of diamond," in *Optical Engineering of Diamond*, R. P. Mildren and J. R. Rabeau, eds. (Wiley-VCH Verlag GmbH, 2013), pp. 1–34.
33. K. C. Lee, B. J. Sussman, J. Nunn, V. O. Lorenz, K. Reim, D. Jaksch, I. A. Walmsley, P. Spizzirri, and S. Prawer, "Comparing phonon dephasing lifetimes in diamond using transient coherent ultrafast phonon spectroscopy," Diam. Relat. Mater. **19**, 1289–1295 (2010).
34. K. Ishioka, M. Hase, M. Kitajima, and H. Petek, "Coherent optical phonons in diamond," Appl. Phys. Lett. **89**, 231916 (2006).
35. A. Shtukenberg, Y. O. Punin, and B. Kahr, *Optically Anomalous Crystals* (Springer, 2007).
36. E. Anastassakis, A. Pinczuk, E. Burstein, F. Pollak, and M. Cardona, "Effect of static uniaxial stress on the Raman spectrum of silicon," Solid State Commun. **88**, 1053–1058 (1993).
37. P. Hess, "The mechanical properties of various chemical vapor deposition diamond structures compared to the ideal single crystal," J. Appl. Phys. **111**, 051101 (2012).
38. O. Kitzler, A. McKay, and R. P. Mildren, "Continuous-wave wavelength conversion for high-power applications using an external cavity diamond Raman laser," Opt. Lett **37**, 2790–2792 (2012).
39. R. J. Williams, J. Nold, M. Strecker, O. Kitzler, A. McKay, T. Schreiber, and R. P. Mildren, "Efficient Raman frequency conversion of high-power fiber lasers in diamond," Laser Photon. Rev. **9**, 405–411 (2015).
40. A. Mckay, O. Kitzler, and R. P. Mildren, "Simultaneous brightness enhancement and wavelength conversion to the eye-safe region in a high-power diamond Raman laser," Laser Photon. Rev. **8**, L37–L41 (2014).
41. A. Sabella, J. A. Piper, and R. P. Mildren, "1240 nm diamond Raman laser operating near the quantum limit," Opt. Lett. **35**, 3874–3876 (2010).
42. A. Sabella, J. A. Piper, and R. P. Mildren, "Efficient conversion of a 1064 μm Nd:YAG laser to the eye-safe region using a diamond Raman laser," Opt. Express **19**, 23554–23560 (2011).
43. J.-P. M. Feve, K. E. Shortoff, M. J. Bohn, and J. K. Brasseur, "High average power diamond Raman laser," Opt. Express **19**, 913–922 (2011).
44. R. P. Mildren, J. E. Butler, and J. R. Rabeau, "CVD-diamond external cavity Raman laser at 573 nm," Opt. Express **16**, 18950–18955 (2008).
45. E. Granados, D. J. Spence, and R. P. Mildren, "Deep ultraviolet diamond Raman laser," Opt. Express **19**, 10857–10863 (2011).
46. D. C. Parrotta, A. J. Kemp, M. D. Dawson, and J. E. Hastie, "Tunable continuous-wave diamond Raman laser," Opt. Express **19**, 24165–24170 (2011).
47. A. Penzkofer, A. Laubereau, and W. Kaiser, "High intensity Raman interactions," Prog. Quantum Electron. **6**, 55–140 (1979).
48. R. Loudon, "The Raman effect in crystals," Adv. Phys. **13**, 423–482 (1964).